energies

MDPI

Article

A Study on Swirling Jets Flow Controlled by Two Tandem Bodies

Minh Duc Le [1,*], Shiferaw Regassa Jufar [2], Dinh Nghia Duong [1] and Thi Phuong Quyen Nguyen [3]

[1] Faculty of Transportation Mechanical Engineering, The University of Danang-University of Science and Technology, 54 Nguyen Luong Bang, Da Nang 550000, Vietnam; ddnghia@dut.udn.vn
[2] Department of Petroleum Engineering, Universiti Teknologi PETRONAS, Persiaran UTP, Seri Iskandar 32610, Perak, Malaysia; shiferaw.jufar@utp.edu.my
[3] Faculty of Project Management, The University of Danang-University of Science and Technology, 54 Nguyen Luong Bang, Da Nang 550000, Vietnam; ntpquyen@dut.udn.vn
* Correspondence: minhducle@dut.udn.vn

Abstract: This study presents the effects of using two centerbodies arranged in tandem on the flow and velocity properties of swirling jets. The centerbodies are installed concentrically downstream of the jets to modify the wake. Smoke flow visualization was employed to illustrate the flow behaviors, while the particle image velocimetry technique was utilized to investigate the velocity fields, turbulent properties, vorticities, and Lagrangian time and length scales. The toroidal recirculation and vortex shedding are found near the field using one centerbody. The recirculation zone is evolved from the edge of the centerbody, while the vortex shedding is formed by the interaction between the central and the annular jets. Since two centerbodies are installed, two four-way saddles are located near the rim of the upstream centerbody to associate two pairs of vortices. A large momentum of the annular jet dominates the flow field; therefore, the central jet forms dual-rotating vortices at downstream centerbody. The turbulent intensity and vorticity along the central axis in the case of two centerbodies are extremely lower than those in the case of one centerbody. Large turbulent intensity and vorticity are located around the shear layers of jets. This promotes a better mixing efficiency of the swirling jets.

Keywords: swirling jet; centerbody; vorticity; turbulent jet; PIV

check for updates

Citation: Le, M.D.; Jufar, S.R.; Duong, D.N.; Nguyen, T.P.Q. A Study on Swirling Jets Flow Controlled by Two Tandem Bodies. *Energies* **2022**, *15*, 3590. https://doi.org/10.3390/en15103590

Academic Editor: Daniele Testi

Received: 3 April 2022
Accepted: 11 May 2022
Published: 13 May 2022

Publisher's Note: MDPI stays neutral with regard to jurisdictional claims in published maps and institutional affiliations.

Copyright: © 2022 by the authors. Licensee MDPI, Basel, Switzerland. This article is an open access article distributed under the terms and conditions of the Creative Commons Attribution (CC BY) license (https://creativecommons.org/licenses/by/4.0/).

1. Introduction

Double-concentric center tube jets are commonly found in many applications to improve mixing and combustion instabilities [1–3], for example, burners, gas turbines, furnaces, mixers, etc. The center tube plays an important role either as a bluff body or as a fuel injection device. The existence of a center jet tube induces a central recirculation zone (RZ) near the wake and associates it with either flame stabilization or mixing capability. The RZ that occurs in the bluff body's wake provides a high rate of momentum and mass exchanges between the central and the annular jet fluids. This configuration is also denoted as a coaxial jet [4,5]. In practical uses, to maintain the long residence mixing time, the central jet fluid with low velocity is injected into the RZ and interacts with the annular jet via diffusion and dispersion. However, beyond a certain value of the central jet velocity, the mixing capability of double-concentric center jets becomes relatively worse.

Next to the applications of using double-concentric jets and a bluff body, another way to improve mixing capabilities and combustion efficiency is the use of swirl, i.e., swirling jet flow. The swirl movement is usually superimposed to a circular jet, resulting in a large RZ with high fluctuation intensities induced near the field. This RZ presents a rich variety of phenomena, e.g., flow characteristics and vortex breakdown. An overview of the engineering applications of swirl is presented in many studies [6–9]. The prominent feature of swirling jets, i.e., high turbulence intensity inside the RZ, is expressed in high physical mechanisms as varying swirl strength. The swirl strength (or swirl rate) can be represented by the swirl number (S) [10]. Following the suggestion of Gupta et al. [10], a

large RZ occurs near the jets' exit when the swirl rate and Reynolds number are higher than certain thresholds of 0.6 and 18,000, respectively. This RZ is characterized as a region with a zero or negative mean velocity. The RZ is separated from the transition region in the downstream wake by a stagnation point. The formation of RZ is closely related to the "vortex breakdown" feature of a swirling jet [11]. Markovich et al. [12] reported the shapes and helical instability modes of large-scale vortical structures of a swirling jet at low and high swirl rates using the 3-D high-speed tomographic PIV technique. The swirl strengths were 0.41 and 1.0, while the Reynolds number was fixed at about 8900. The vortex breakdown recirculation was fully observed near the wake region as a toroidal bubble with high turbulence intensity in the case of high swirl strength, while the axial velocity was decreased with increasing axial distance.

Generally, in many industrial applications, an annular swirling jet in combination with a blockage ratio (B) of the bluff body is commonly used to modify flow patterns to provide the same effects as that of a free swirling jet. A bluff body partially blocks the annular jet flow with a large Reynolds number (i.e., Re > 1000), resulting in the formation of the RZ downstream of the bluff body, e.g., a separated toroidal wake and a merged toroidal wake [13–17]. Therefore, mass transfer and mixing are enhanced in the near field of the jet flow consequently. Compared computational fluid dynamics (CFD) and experiments on the near field of swirling jets in terms of RZ characteristics were also reported recently [18,19]. An overview of relevant literature publications is presented in Table 1.

Table 1. Overview of literature publications on annular swirling jet with a bluff body installed.

Ref. No.	B	u_c [m/s]	Re	S	Method	Flow Features
[18]	0.16	4.67	7531	1.4	RANS; DDES; stereo-PIV (non-reacting and reacting swirling flow)	Central RZ surrounded by shear layers
[19]	0.19 0.39	4.22	1222	4.08	LES; PIV	RZ is affected by swirl strength RZ size is dominated by bluff body
[20]	0.42	0.92	8300	0.36	3-D tomographic PIV	Vortex breakdown RZ and helix structure
[21]	0.17	15	21,800	0–1.4	Stereoscopic PIV; proper orthogonal decomposition; phase-average	Vortex breakdown RZ and precessing vortex core (PVC)
[22]	0.23	-	(0–6000)	<0.07 (0.07–0.075) (0.075–0.1) (0.1–0.16) (0.16–0.3) >0.3	Smoke-streak flow visualization and laser Doppler anemometry (LDA)	Vortex shedding Transition Prepenetration Penetration Vortex breakdown Attachment

For practical nozzles in applications, to ensure that the formation of the RZ occurs in the wake of a single swirling jet, the Reynolds and swirl numbers must be operated at higher than 18,000 and 0.6, respectively [10]; however, for Reynolds numbers below 1000, based on mean velocity measured at the jet exit and the diameter of the jets, i.e., small-scale engineering applications, to improve the mixing capabilities and combustion efficiency, combining the swirling double-concentric jets and a large blockage bluff body could be a good way to create the RZ near the wake of the jets' exits. For instance, Huang and Tsai [17] combined swirling double-concentric jets and a large concentric bluff body. They performed smoke flow visualization, laser Doppler velocimetry (LDV), and concentration detection techniques to obtain the flow structures, velocity vector fields and turbulence features, and mixing capabilities of swirling jets in the domains of annular jet Reynolds number (Rea) and central jet Reynolds number (Rec). The blockage disk ratio was 0.563. Interestingly, the flow modes of swirling double-concentric jets identified in the RZ were single-bubble, dual

rings, vortex breakdown, and vortex shedding in the range of (Rec, S) < (1000, 0.5). The RZ was easily observed in the wake of the swirling jets; however, as the central jet penetrated the RZ (i.e., Rec > 500), the fluctuation intensities were not high because of less dispersion of central jet fluids into the RZ. Consequently, the mixing index detected in the jets' wake was not adequately high.

The disadvantage of using a single control disk to modify the jets' wake was appropriately solved by Huang and Yen [23]. They reported a passive control method using a dual-blockage disk arranged in tandem (i.e., 30 mm diameter upstream disk and 14 mm diameter downstream disk) to adjust the flow behaviors in the wake of jets. To reveal the influences of using a dual-blockage disk on flow characteristics, especially the distance between the two circular disks, the smoke flow visualization and PIV methods were employed at a low value of annular jet Reynolds number. The annular jet Reynolds number (Rea) and swirl rate (S) were about 218 and 0.194, respectively. The flow fields were identified as natural state, bubble extension, bubble escape, bubble encapsulation, and gap flow. Apparently, a high mixing index was obtained near the jets' wake, with a low annulus Reynolds number (i.e., Rea = 218) and the normalized axial level between the disks maintained within $0.1 \leq H/D \leq 1.4$ appropriately.

To fully understand the flow behaviors near field of swirling double-concentric jets in a wide range of central jet and annulus jet velocities by taking advances of Huang and Yen's study [23], Huang et al. [24] experimentally performed smoke-wire laser-assisted flow visualization in the domain of (Rec, Rea) $\leq$ (1000, 1000). Several flow characteristic modes were investigated, i.e., *annular-jet-dominated wake*, *central-jet-dominated wake*, *central-jet-dominated flow*, and *high-turbulence swirling wake*. The same authors [25] revealed the velocity characteristics and mixing capabilities of swirling double-concentric jets by using the PIV technique and concentration detection method for Rec < 180 and Rea $\leq$ 1000. They found that, at low Rec, (a) the *vortical wake* feature is formed as (Rea, S) < (270, 0.243), i.e., *annular-jet-dominated wake* mode, while the *turbulent wake* behavior occurs as (Rea, S) > (270, 0.243), i.e., *high-turbulence swirling wake* mode, and (b) the mixing capability of the swirling double-concentric jets is improved. Continuing to investigate the velocity and turbulent properties as well as mixing indexes of the swirling double-concentric jets, Duc et al. [26] performed PIV and gas concentration measurements on the same experimental configuration for Rec < 1000, Rea < 270, and S < 0.243 corresponding to the flow modes of *annular-jet-dominated wake*, *central-jet-dominated wake*, and *central-jet-dominated flow* [24].

To continue the previous works of Huang et al. [24,25] and Duc et al. [26], this study presents the flow behaviors and turbulence features of swirling jets modulated by two centerbodies arranged in tandem. The experiments were employed for the central jet Reynolds number, annular jet Reynolds number, and swirl number within the ranges of 200 < Rec < 400, 260 < Rea < 700, and 0.234 < S < 0.483, respectively. This condition of flow was classified as the *high-turbulence swirling wake* [24]. Since large Reynolds numbers may not be available for practical uses, the formation of smoke-streak flow images, velocity vector fields, streamlines, fluctuation intensities, vorticities, and Lagrangian time and length scale were reported to illustrate the essential understanding of coherent structures characteristics, which affect the mixing processes and combustion capabilities in many small-scale combustions or mixing devices.

2. Methodologies

2.1. Experimental Apparatus

The schematic of the experimental configuration is shown in Figure 1. This setup is as same as that presented in Duc et al. [26]. To investigate the flow behaviors and velocity characteristics in the jets' wake, two independent systems of jets combined with two bluff bodies were installed concentrically. The jet systems consisted of central and annular air passages. The centerbodies, i.e., two stainless-steel circular disks arranged in tandem (i.e., 30 mm and 14 mm in diameter, respectively), were used to modify the flow structures near the jet exits. A nozzle assembly connected to a stainless-steel tube was used

to deliver the central jet fluid. The tube (i.e., central jet tube) had a 600 mm length and a 5 mm inner diameter. As recommended by Huang and Yen [23], the upstream centerbody (named CD1) was installed at the end of the central jet tube (i.e., the central jet's exit), while the downstream centerbody (named CD2) was placed horizontally at H/D = 30% away from CD1. CD1 and CD2 were kept parallel using two rods (1 mm diameter and made of stainless steel). The size of rods was selected to avoid the vortex shedding induced behind its body as the jets were released [24]. This configuration is to ensure that the mixing could be improved by combining the annular swirling jet, central jet, and centerbodies [23].

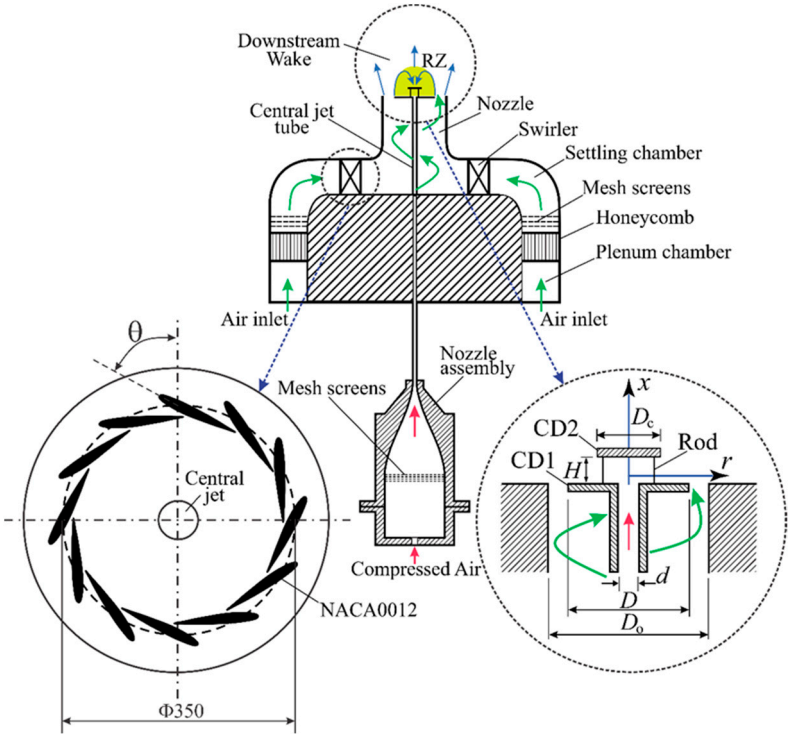

Figure 1. Schematic of the experimental setup.

The annular jet fluid was separately provided to the downstream wake by a set of a blower, an acoustical filter, a pressure regulator, and a rotameter. The rotameter was used to adjust the flow rate of the annular jet. In the test rig, a set of honeycombs and mesh screens was used to condition the flow before it reached the nozzle exit, while a swirler was installed to transmit the swirl motion into the annular jet fluid. A tangent velocity component was generated by a swirler as the air-inlet flow went through a system of NACA 0012 airfoils with a deflection angle of 70°, and those airfoils were located in a pitch circle diameter of 350 mm, as shown in Figure 1. Before the swirling annular airflow issued from the annular jet, it was accelerated by passing a nozzle (9.0 contraction ratio and 40 mm diameter). The hydraulic diameter of the annular jet is D_h = 10 mm.

The coordinate system origin was set to the central jet tube plane on the central jet's exit (Figure 1). The x-coordinate pointed in the axial direction, while the r-coordinate indicated the radial direction. The swirl number (S), as shown in Equation (1), which was the ratio of the axial flux of tangential momentum to the axial flux of axial momentum [10], was defined:

$$S = \int_{\frac{D}{2}}^{\frac{D_0}{2}} uwr^2 dr \Big/ \frac{D_m}{2} \int_{\frac{D}{2}}^{\frac{D_0}{2}} u^2 r dr \quad (1)$$

where u was the axial velocity and w was the azimuthal velocity. The axial and azimuthal velocity components were estimated experimentally by a laser Doppler velocimeter (LDV) technique at the Thermal Science and Fluid Mechanics Laboratory (National Taiwan University of Science and Technology, Taipei, Taiwan). The swirl number was adjusted by

changing the annular jet Reynolds numbers. The swirl rate was operated in the range of $0.234 < S < 0.483$ in this study.

2.2. Flow Visualization and PIV Measurement

2.2.1. Flow Visualization

A traditional smoke flow image visualization method based on the investigation of Mie [27] was operated experimentally. To create the smoke-streak flow patterns, a 100 mm diameter tungsten-steel wire was inserted at $x/D = 0.03$ in the symmetry plane across the jets' outlet. With this wire diameter, the Reynolds number was guaranteed below 40 and, therefore, it might have been possible to avoid the phenomenon of vortex shedding caused by the wire downstream [26,28]. This tungsten wire was linked with a heating power supply. The mineral oil was used to provide smoke streaks in the downstream wakes by adjusting the heating power supply. A Malvern 2600C Particle Analyzer (Malvern Panalytical Ltd., Malvern, UK) was used to detect the particle diameter based on Sauter Mean Diameter (*SMD*) method [9]. The *SMD* number was defined as follows [29]:

$$SMD = \frac{\int_{d_{min}}^{d_{max}} d^3 p(d) \mathrm{d}d}{\int_{d_{min}}^{d_{max}} d^2 p(d) \mathrm{d}d} \quad (2)$$

where d, $d_{\max}$, and $d_{\min}$ were the particle diameter and the maximum and minimum diameters of particle distribution, respectively. $p(d)$ was the probability density function (PDF) of particle diameter d. The SDM was estimated at about 1.7×0.3 µm, while the mist density of kerosene oil was about 5.31 kg/m^3. The oil aerosols had a Stokes number on the order of 0.001, which is substantially lower than one. Hence, the smoke particles should follow the flow, as expected. A double-pulsed laser (LDY 300, Litron Laser Ltd., Warwickshire, UK) was used to provide the laser-light sheet. A 0.5 mm thick laser-light sheet was oriented to the flow field's symmetrical plane. There were two laser modes available: single-pulse and double-pulse. The continuous mode (single-pulsed mode) was used to visualize the flow in the jets' wake. A CMOS camera (Model IDT Y4-S1, Taipei, Taiwan) was used to capture smoke flow images. The specifications of the double-pulsed laser and high-speed camera are presented in Tables 2 and 3, respectively.

To perform smoke flow image visualization, the double-pulsed laser was set in single-pulsed mode and the framing rate of the high-speed camera was set at 30 fps. The exposure time of instantaneous images was 0.02 s.

Table 2. Specifications of dual-head diode-pumped Nd: YLF laser.

Property	Value
Manufacturer	Litron Lasers Ltd.
Model (a dual-cavity system)	LDY300
Wavelength (nm)	527
Pulsing rate (each laser head) (kHz)	0.2–20
Output energy @ 1 kHz, at 527 nm (each laser head) (mJ)	10
Pulse stability (%)	±1
Pulse width at 1 kHz (ns)	~150

Table 3. Specifications of high-speed camera.

Property	Value
Manufacturer	Integrated Design Tools, Inc. (IDT).
Model	Y 4-S1
Maximum resolution (pixels)	1.024 × 1.024
Maximum FPS @ Max. Res. (fps)	3000
Plus mode @ 1024 × 1024 pixels (fps)	6000
Maximum frame rate @ 1024 × 16 pixels (fps)	72,000
Minimum exposure time (μs)	1
Sensitivity ASA	6000 ISO Mono and 2000 ISO color
Sensor type	CMOS
Sensor size (mm)	13.9 × 13.9
Image size (megapixel)	1.0
Pixel size (μm)	13.68 × 13.68
Pixel depth	10-bit mono and 30-bit color

2.2.2. PIV Technique

Particle image velocimetry (PIV) was employed to characterize the velocity vectors and streamlines near the wake of the swirling jets. Figure 2 shows a 2-D PIV arrangement composed of a double-pulsed YLF laser, a synchronizer, a CMOS camera, and an image processing system with an installed commercial PIV analysis software (proVISION-XS PIV v3.12.1, Taipei, Taiwan). The PIV sofware was employed to reveal the velocity and turbulent properties in the 2-D symmetry plane downstream wake of the jets. A large cover box (1200 mm × 1200 mm × 1200 mm, free at the bottom and the top) was used to avoid the effects of ambient disturbance on the flow field during the experiments. To observe the velocity measurement, the double-pulse mode was required for the laser. The time interval between the two-cavity pulsed lasers was set as 50 μs. This separation time was adjusted experimentally to obtain a good calculation of turbulent intensity, time scales, and length scales [30]. The speed of the CMOS camera was optimized and finally set at 2280 fps at the camera resolution of 750 × 750 pixels (i.e., 72 mm × 72 mm in reality space). The spatial resolution was 96 μm/pixel, consequently.

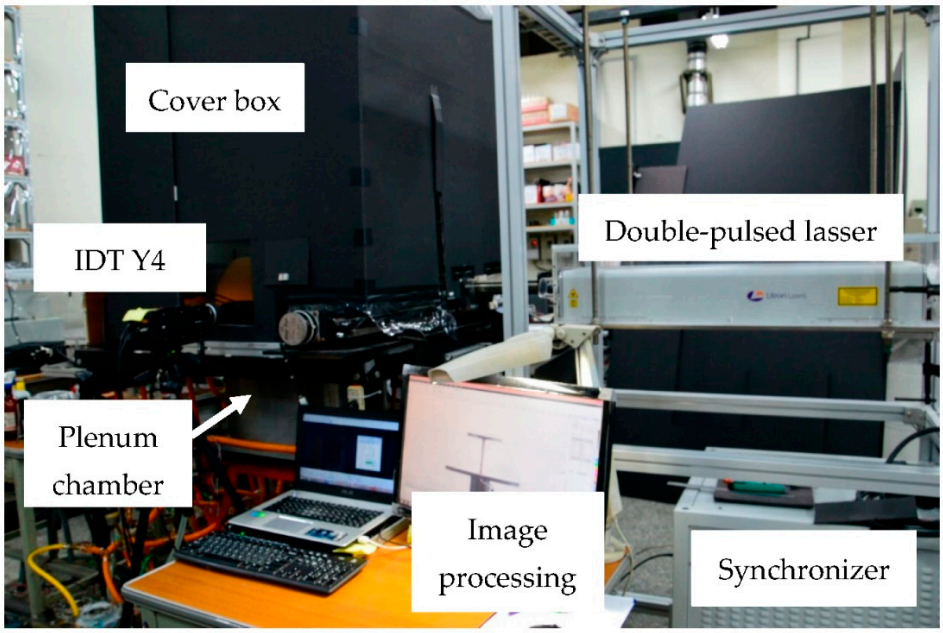

Figure 2. Two-dimensional high-speed PIV system setup.

The cross-correlation method was embedded in a commercial PIV software to estimate the velocity field characteristics [31]. The local-averaged displacement value of the particles in a group of two consecutive images was estimated by PIV software in an interrogation window size (IWS). To enhance the precision of the velocity calculations, the IWS was found analytically by processing photos with correlation window sizes ranging from a minimum value of 32 pixels × 32 pixels to a maximum value of 128 pixels × 128 pixels. The final IWS was set at 32 pixels × 32 pixels, which served no noticeable specious vectors. The interrogation regions overlapped by 50% in both axial and radial directions which were enabled to yield a velocity vector field with a total of 180 × 180 vectors (in the 2-D median plane of the swirling double-concentric jets). The measurement points were very dense, but for clarity of presentation, the surplus velocity vectors were deleted from the figures. The convergence method was performed experimentally, and finally, there were 8000 image pairs obtained to produce the time-averaged values in terms of reducing the processing time.

As recommended by Westerweel [31], the particle displacement in two successive images should be kept lower than one-fourth of the interrogation spot length to reduce the velocity bias in the areas that contain large velocity gradients. Error check routines and interpolation methods were served to determine outliers. By changing the seeding density, the number of particle–image pairs per interrogation spot was kept higher than four to increase measurement reliability.

2.2.3. Uncertainty of Measurements

The uncertainties of the measurements were estimated following the suggestion of Steele et al. [32]. A total uncertainty of the variable parameters can be obtained through combining systematic and random errors, i.e., $E = \left(B^2 + (tS_D)^2\right)^{1/2}$, where B is the systematic uncertainty, S_D is the standard deviation of the mean, and t is the degree of freedom. The degree of freedom was about 1.96 with a 95% confidence level. The systematic uncertainty was calculated from the calibration data and previous tests, whereas the standard deviation of mean was obtained from the raw experimental data. In this study, the uncertainty of velocity obtained by PIV technique was estimated within ±2% [32,33]. The uncertainties of the fluctuation intensity and vorticity were evaluated at approximately ±2.5% and ±4%, respectively [33]. The uncertainty of the flow rate measured by the rotameters was about ±2% of the full scale.

3. Results and Discussion

3.1. Smoke-Streak Flow Patterns

Figure 3 presents the 2-D instantaneous smoke flow patterns in the wake of swirling double-concentric jets using one centerbody and two centerbodies at Re_c = 280, Re_a = 480, and S = 0.432.

Using a centerbody (i.e., CD1) shown in Figure 3a, the central jet evolves from the central hole of CD1, shoots downstream directly, and mixes with the swirling jet-like flow. The swirling jet-like flow occurs by combining the effects of the central jet fluid, the swirling annular flow, and the ambient air entrainment. A pair of counter-rotating inner vortices (V1, V2) and a pair of counter-rotating outer vortices (V3, V4) exist near the jets' exit downstream of CD1 due to the effects of the centerbody. The RZ is represented by the pairs of vortices (V1, V2), i.e., called inner vortices, and (V3, V4), i.e., called outer vortices, and appears within the range of $x/D < 0.5$. Large eddies of fluids break up into small eddies at $x/D > 1.0$ due to the increase in air entrainment in the downstream wake. It is seen that the interaction between the central jet and the RZ is not strong enough, as the mass and momentum of central jet fluids travel to the downstream wake immediately after issuing from the central hole of CD1.

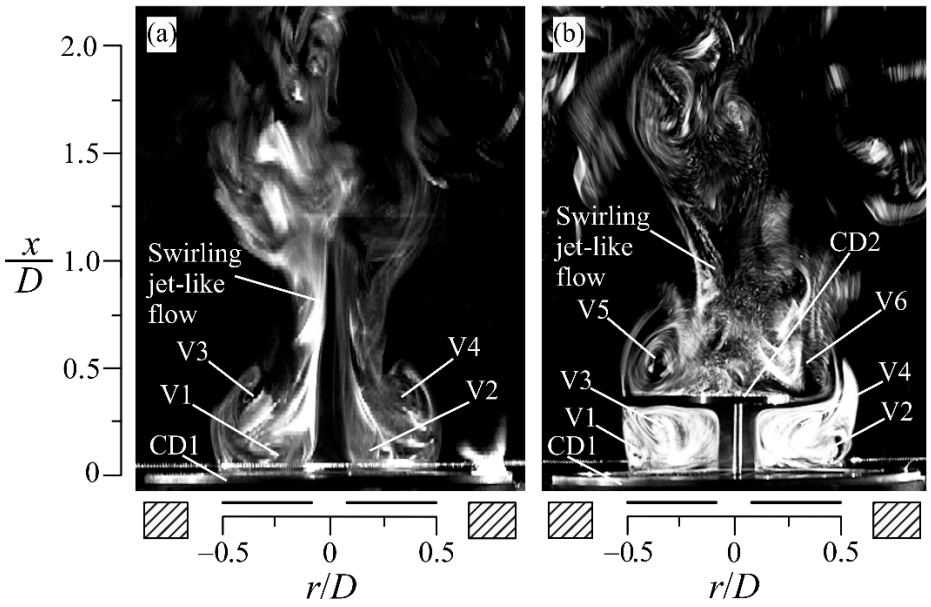

Figure 3. Instantaneous smoke flow patterns in axisymmetry plane of swirling double-concentric jets. Re_c = 280, Re_a = 480, and S = 0.432. (**a**) One centerbody, (**b**) two centerbodies. Exposure time: 20 ms.

To modify the flow structures shown in Figure 3a, a dual centerbody arranged in tandem was used. In Figure 3b, a large RZ is located downstream of the jets' exit. This RZ is a combination of two pairs of vortices that occur in between the central bodies and a pair of vortices evolved at the edge of CD2. This phenomenon is explained as the central jet releases from the central tube, impinges CD2, bifurcates radially, and then creates two pairs of counter-rotating inner vortices (V1, V2) and outer vortices (V3, V4). These vortices' lengths in the axial direction are smaller than those that appeared in Figure 3a. Due to the existence of CD2, a part of the bifurcated central jet fluids rolls up and forms into a pair of counter-rotating vortices (V5, V6). An unsteady swirling jet-like flow occurs at the top of the recirculating vortical structure (V5, V6) (at about $x/D \approx 0.7$), goes downstream, and rotates in the same direction as that of the annular jet. It means that, in the axial direction, the RZ size observed in the case of using a dual centerbody (Figure 3b) is longer than that in the case of using one centerbody (Figure 3a). In addition, the size of the RZ increases with increasing the central jet Reynolds numbers. This is because the central jet fluid impinges CD2 and then it bifurcates radially before turning upward at a large Rec. This bifurcated jet induces a shear layer along with the vortices (V5, V6), as the annular swirling flow has larger momentum than the central jet fluids. In other words, the RZ is encapsulated by the annular swirling jet fluids. At the axial distance of $x/D \geq 1.5$, the flow structures become more turbulent than those shown in Figure 3a. Similar flow structures are shown in Figure 3b, i.e., outer vortices (V1, V2) and inner vortices (V3, V4) are located in the gap of the center bodies. A pair of vortices (V5, V6) and a swirling jet-like flow can be found as varying Re_c and Re_a within the range of $200 < Re_c < 400$ and $260 < Re_a < 700$, respectively.

3.2. Velocity Vectors and Streamlines

Figure 4 exhibits the time-averaged velocity vectors field and streamlines measured at Re_c = 280, Re_a = 480, and S = 0.432 in the jets' wake controlled by a dual centerbody arranged in tandem. As shown in Figure 4a (CD1 installed), two pairs of counter-rotating vortices (V1, V2) and (V3, V4) are formed near the jets' exit and downstream of CD1. This is because a part of the central jet fluids interacts, i.e., exchanges momentum, with the annular swirling jets as the jets pass through CD1. All streamlines issued from the central hole of CD1 go straightforward downstream and do not meet along the x-direction and then slightly deflect due to the effects of the swirling annular jet at about $x/D > 1.0$. The mixing index between the free jet and the annular swirling jet is not good along the central jet axis since no stagnation

point exists on the *x*-axis, as clearly mentioned by Huang and Tsai [16]. The behaviors of flow shown in Figure 3a are well revealed quantitatively in Figure 4a.

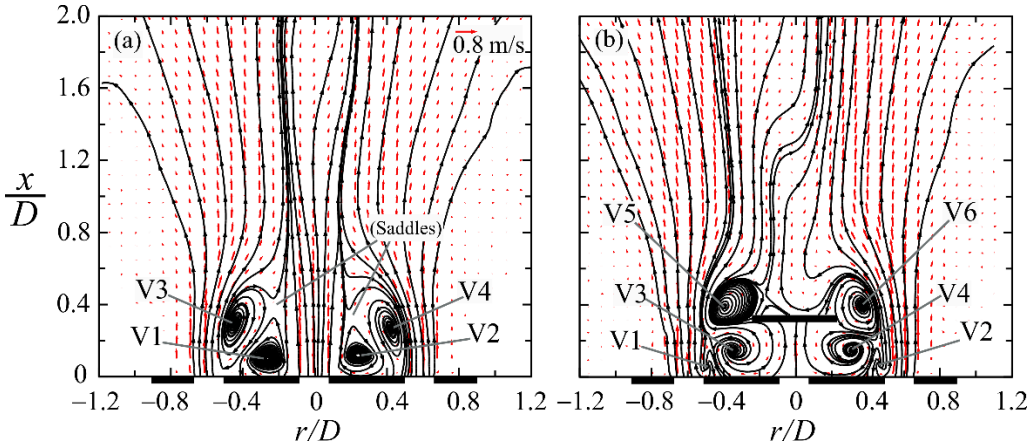

Figure 4. Velocity vectors and streamline patterns of swirling double-concentric jets. Re_c = 280, Re_a = 480, and S = 0.432. (**a**) One centerbody, (**b**) two centerbodies.

Figure 4b presents the time-averaged velocity fields (i.e., vectors and streamlines) taken at Re_c = 280, Re_a = 480, and S = 0.432. In this case, a pair of inner counter-rotating vortices (V1, V2) and a pair of outer counter-rotating vortices (V3, V4) are induced and located between CD1 and CD2 as same as those represented in Figure 3b. A counter-rotating vortice pair appears near the rim of CD2, i.e., (V5, V6), and the forward flow exists in the downstream wake of CD2. A stagnation point exists downstream of CD2 to associate the vortices (V5, V6). The swirling jet-like flow in Figure 4b is wider than that in Figure 4a on the *r* direction. This means that the RZ length in the case of a dual centerbody is greater than that in the case of one centerbody. Therefore, there is an improvement in mass and momentum transfer from the central jet fluid and annular swirling jet compared to that which occurs in the case of using only one centerbody, shown in Figure 4a. This appearance of flow is aligned with that of the flow patterns depicted in Figure 3b observed at 200 < Re_c < 400, 260 < Re_a < 700, and 0.234 < S < 0.483. This is termed *turbulent forward-flow wake*.

3.3. Characteristics of Fluctuation Intensities

Figures 5 and 6 present the time-averaged streamwise (axial) fluctuation intensity and spanwise (radial) fluctuation intensity contours at Re_c = 280, Re_a = 480, and S = 0.432. The fluctuation contours of velocity are used to identify the location and extent of flow behaviors (i.e., potential core jet and shear layer).

Due to the jets accelerating and decelerating in the wake, as shown in Figure 5a, i.e., the one-centerbody case, the streamwise fluctuation intensities (u'/u_c) are significantly enhanced around the jets' exit region and then decay gradually downstream with increasing axial and radial distances. The inner shear layer evolves along the boundary of the central jet column (i.e., jet width), while the outer shear layer exists along the regions corresponding to the vortices (V3, V4) shown in Figure 4a. These shear layers are induced by the difference in velocity between two nearby regions. Apparently, using two centerbodies, Figure 5b, the axial fluctuation intensities u'/u_c exhibit lower values than those in the case of using one centerbody (Figure 5a). This is because the mass and momentum of the central jet are transferred radially due to the existence of vortices (V1, V2), (V3, V4), and (V5, V6) shown in Figure 4b. Around the shear-layer regions induced by the annular jet, i.e., the outer shear layer, as shown in Figure 5b, the values of u'/u_c attain up to 0.24. It can be seen in Figure 5b that the low turbulent intensity exhibited surrounding the wake of CD2 is caused by the unstable motion of the swirling jet-like flow (shown in Figure 4b). Consequently, the

values of u'/u_c are very low along the central axis in the downstream wake as compared to those in Figure 5a, i.e., downstream of CD2, u'/u_c presents values of up to 0.08.

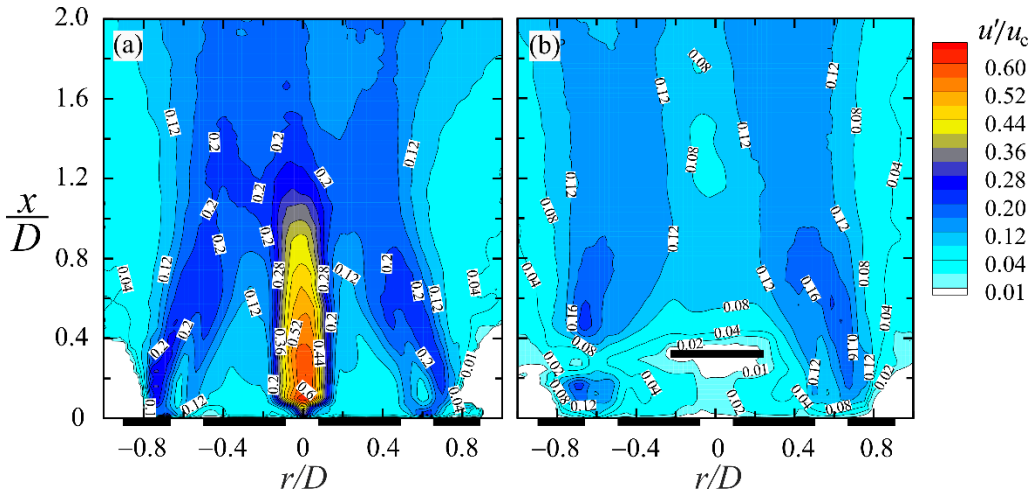

Figure 5. Axial fluctuation velocity contours of swirling double-concentric jets. Re_c = 280. Re_c = 280, Re_a = 480, and S = 0.432. (**a**) One centerbody, (**b**) two centerbodies.

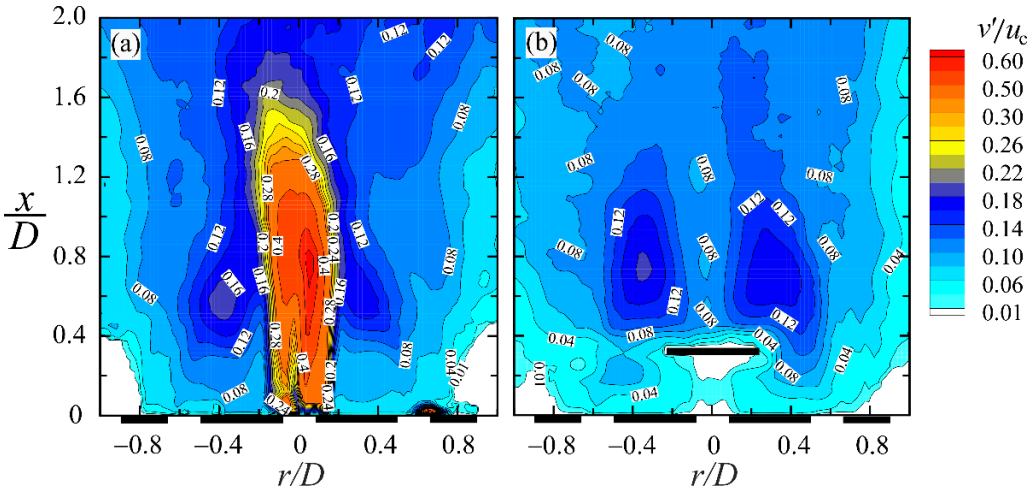

Figure 6. Radial fluctuation velocity contours of swirling double-concentric jets. Re_c = 280, Re_a = 480, and S = 0.432. (**a**) One centerbody, (**b**) two centerbodies.

As shown in Figure 6a, i.e., the one-centerbody case, similar results to those occurring in Figure 5a are observed, with the largest value of v'/u_c up to about 0.6 around the region within $(-0.2, 0) < (r/D, x/D) < (0.2, 1.6)$. The large areas located on both sides of the x-axis within $-0.6 < r/D < -0.2$, $0.2 < r/D < 0.6$, and $0.4 < x/D < 2.0$, which correspond to the regions where the pairs of (V1, V2) and (V3, V4) appear in Figures 3a and 4a, present values of v'/u_c up to 0.2. At $|r/D| > 0.6$, the radial fluctuation intensity value v'/u_c ecreases with increasing radial distance. In the case of two disks, as shown in Figure 6b, the largest radial fluctuation intensity value v'/u_c attains up to about 18% concentrated around the (V5, V6) (Figures 3b and 4b) within $-0.60 < r/D < -0.15$, $0.15 < r/D < 0.60$, and $0.4 < x/D < 1.2$. The radial fluctuation intensities (Figure 6b) in the radial direction are greater than those in the axial direction (Figure 5b). It can be explained that, as the wake is modified by two centerbodies, the mass and momentum are dramatically transported from the axial direction to the radial direction, resulting in the improvement of the mixing capability in the RZ.

3.4. Velocity Profiles and Turbulence Characteristics

Figure 7 presents the normalized axial and radial mean velocities and fluctuation intensities on the x-axis of swirling double-concentric jets at Re_c = 280, Re_a = 480, and S = 0.432. They are normalized by the central jet exit velocity. In Figure 7a, the axial mean velocities $(\overline{u}/u_c)$ of the one-centerbody case exhibit significantly larger values than those of the two-centerbodies case. This can be explained in that the central jet mostly transports the momentum to downstream jets' wake in the one-centerbody case, whereas the central jet impinges CD2 before bifurcating radially in the two-centerbodies case. Therefore, the axial momentum of the central jet is significantly decreased as the CD2 installed. In the one-centerbody case, $(\overline{u}/u_c)$ exhibits high values near the jets' exit and then decreases gradually with increasing axial level. For instance, at x/D = 0.4, $(\overline{u}/u_c) \approx 0.65$ (Figure 7a). In the turbulent forward-flow wake region of the two-centerbodies case, $\overline{u}/u_c$ has low positive values because the swirling jet-like flow goes downstream, as shown in Figure 4b. In Figure 7b, the values of normalized radial mean velocities $(\overline{v}/u_c)$ for the one-centerbody case are approximately zero along the x-axis. Because the flow fields are almost axisymmetric, the time-averaged quantities of $(\overline{v}/u_c)$ are almost zero.

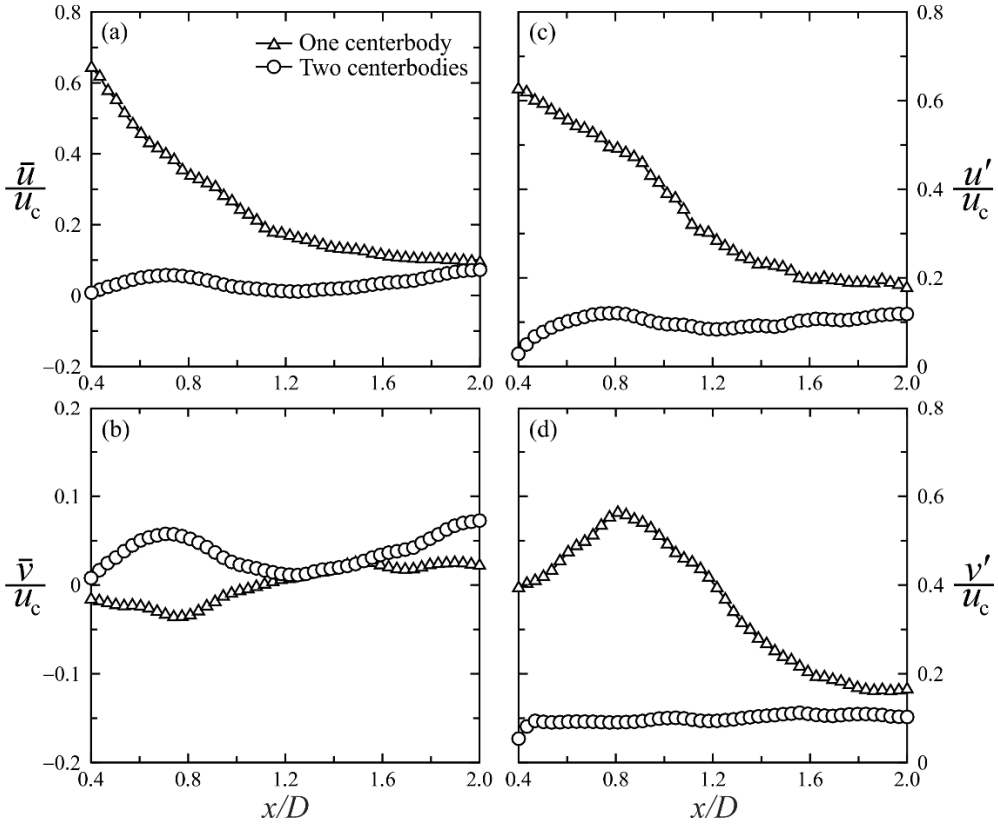

Figure 7. Normalized time-averaged velocities and velocity fluctuation intensities along central line. Re_c = 280, Re_a = 480, and S = 0.432. (**a**) Axial mean velocities, (**b**) radial mean velocities, (**c**) axial fluctuation intensities, (**d**) radial fluctuation intensities.

Figure 7c,d describe the normalized axial and radial fluctuation velocities on the x-axis of the swirling jets. In Figure 7c, the axial fluctuation velocities (u'/u_c) of the one-centerbody case are substantially higher than those of the two-centerbodies case. In Figure 7d, similar to what occurred in Figure 7c, the normalized radial fluctuation velocities (v'/u_c) in the one-centerbody case report significantly higher values than those in the two-centerbody case. On the x-axis of the turbulent forward-flow wake, v'/u_c exhibits a scenario with a magnitude order similar to that presented in Figure 7c.

Figure 8a,b show the radial distributions of the normalized axial mean velocities $(\overline{u}/u_c)$ of swirling jets at the two axial stages x/D = 0.5 and 1.5, respectively. They are normalized by the central jet exit velocity. The axial mean velocities $(\overline{u}/u_c)$ increase with increasing the annular jet Reynolds number and swirl rate in both cases of one- and two-centerbody. All the profiles of $(\overline{u}/u_c)$ display two peaks. With respect to the x-axis, these profiles are nearly symmetrical. In the one-centerbody case, the peak values of the axial mean velocities $\overline{u}/u_c$ are always located in the central region (i.e., $|r/D| \leq 0.2$) and the regions between the shear layers start from the bound of CD1 and the outer bound of the annular jet. Within the range $|r/D| \leq 0.2$, the peak value of $\overline{u}/u_c$ decreases rapidly with increasing the axial level. In the two-centerbodies case, at $|r/D| \leq 0.2$, $\overline{u}/u_c$ retains particularly low positive values in the turbulent forward-flow wake at all three axial levels because no recirculation flow occurs in the wake of CD2.

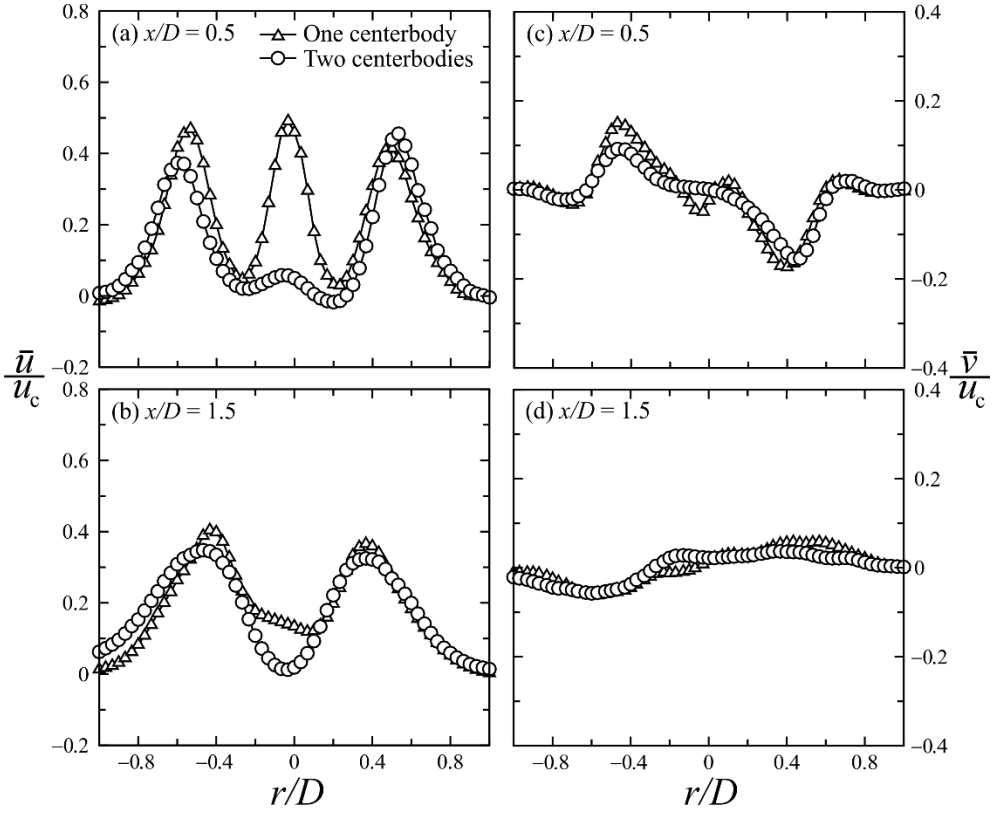

Figure 8. Radial distributions of normalized time-averaged velocities at x/D = 0.5 and 1.5. Re_c = 280, Re_a = 480, and S = 0.432. (**a**,**b**) Axial component, (**c**,**d**) radial component.

Figure 9a,b show the normalized axial fluctuation velocities u'/u_c distributed in the radial direction at axial stages x/D = 0.5 and 1.5, respectively. At low axial levels, the axial fluctuation velocity profile exhibits quad-peak values in both the one- and two-centerbody cases. These peak values of fluctuation velocities exhibit features of inner and outer local maxima. For each dual-peak velocity profile shown in Figure 9a,b, two inversion points (i.e., inner and outer) appear to associate each axial mean velocity peak. These inversion points induce the local maxima of fluctuation intensities. In the case of one centerbody, (u'/u_c) exhibits high values in the range of $-0.2 \leq r/D \leq 0.2$ around the center jet axis and decreases with increasing the axial level. For instance, the maximum values of u'/u_c are about 0.55 (Figure 9a) and 0.24 (Figure 9b) at $(r/D, x/D) \approx (0, 0.5)$ and $(-0.1, 1.5)$, respectively. In the case of two centerbodies, u'/u_c exhibits lower values than those in the case of one centerbody in the region near the x-axis.

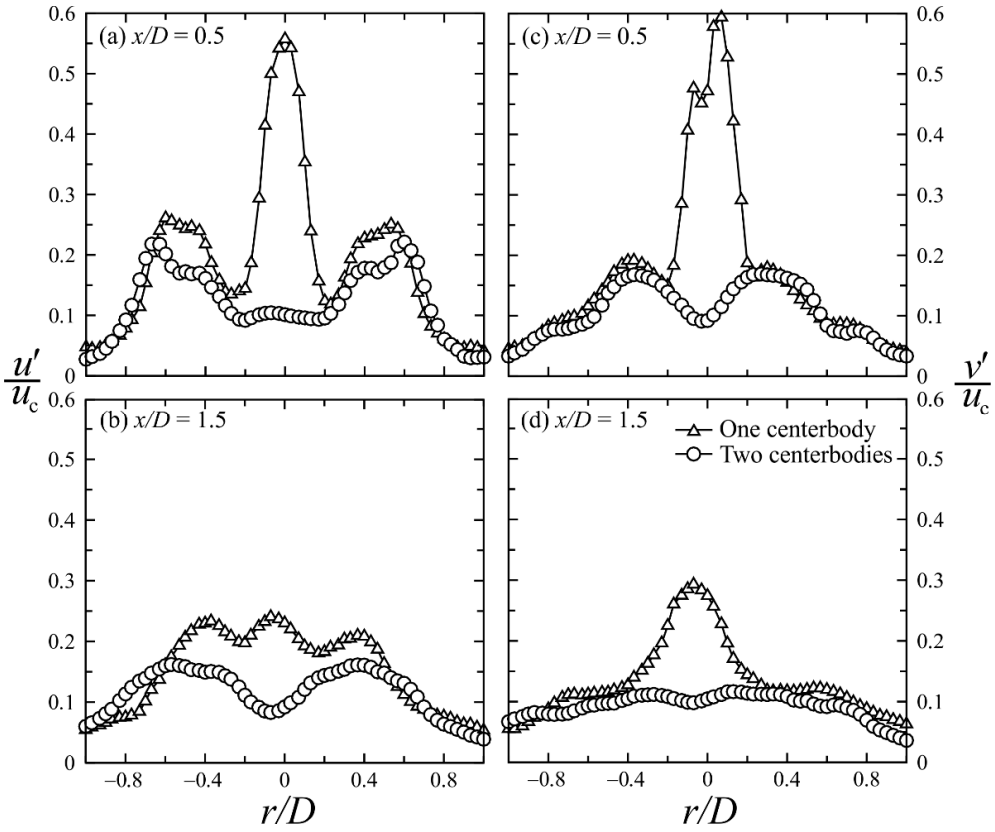

Figure 9. Radial distributions of normalized fluctuation intensities at x/D = 0.5 and 1.5. Re_c = 280, Re_a = 480, and S = 0.432. (**a**,**b**) Axial component, (**c**,**d**) radial component.

Figure 9c,d present the normalized radial fluctuation intensities (v'/u_c) distributed in the radial direction at x/D = 0.5 and 1.5, respectively. Similar to what occurred in Figure 9a,b for both the one- and two-centerbody cases, the radial fluctuation intensities (v'/u_c) decrease with increasing axial distance. The profile of (v'/u_c) in the turbulent forward-flow wake displays a curve similar to that in the case of one centerbody at $|r/D| > 0.2$ and $x/D < 1.5$. Consequently, the axial momentum of the central jet fluids is transferred to the radial direction when CD2 is installed. In other words, this transformation of momentum induces a relative rise in the axial and radial fluctuation intensities in the jets' wake region. Therefore, the mass diffusion between the central jet and the annular jet is increased.

Figure 10 presents the radial distributions of normalized time-averaged vorticity $(\Omega/(u_c/d))$ at various axial levels, i.e., x/D = 0.4, 0.6, 0.8, and 1.0, of jets' wake controlled by one and two centerbodies. The vorticities (Ω) are normalized by (u_c/d). The axial stages are selected to reveal the vorticity inside and outside of the RZ. The vortices exhibit high values around the shear layer since a large difference in velocity gradient occurred. The negative value of vorticity presents a clockwise rotation, while the positive value of vorticity showed a counterclockwise rotation. Within the RZ, as shown in Figure 10a, i.e., x/D = 0.4, in the case of using one centerbody, it is seen that the dual-peak values of vorticity occurred on the inner shear layers of the central jet at $r/D = \pm 0.25$, while other dual-peak values are located on the outer shear layers of the swirling jet at $r/D = \pm 0.5$. Outside of the shear layers, the vorticity is gradually decreased due to the low-velocity gradient existence. In the case of two centerbodies, the vorticity exhibits almost null around $|r/D| \leq 0.25$ due to the effects of CD2 on the wake. This is because there was almost no flow found in the downstream wake of CD2, as shown in Figure 4b. However, as the axial distance increases to x/D = 0.6 (Figure 10b), the vorticity is slightly increased in the downstream wake of CD2 since the flow starts to accelerate downstream of the stagnation point (Figure 4b). As $|r/D| > 0.25$, the largest vorticity occurs on the outer shear layers as the swirling annular

jet starts from the bound of the annular jet, the same as those occurring in the case of one centerbody. For instance, the peak values of $\Omega/(u_c/d)$ are located around $r/D = \pm 0.5$ and ± 0.7. Apparently, the maximum value of $\Omega/(u_c/d)$ in the case of two centerbodies is greater than that in the case of one centerbody. In other words, these peaks of $\Omega/(u_c/d)$ are represented for a high rotational rate of fluids. The maximum value of $\Omega/(u_c/d)$ on the shear layers is gradually decreased with increasing the axial distance, as shown in Figure 10a–d. In addition, the peaks are slightly moved towards the central jet with the increasing axial distance and the vorticity values downstream of the stagnation point are increased since the swirling jet-like flow occurs in the wake, as shown in Figures 3b and 4b. In addition, outside of the RZ, as shown in Figure 10c,d, e.g., $x/D \geq 0.8$ and $|r/D| > 0.25$, the vorticity curve in the case of two centerbodies displays a scenario similar to that in the case of one centerbody.

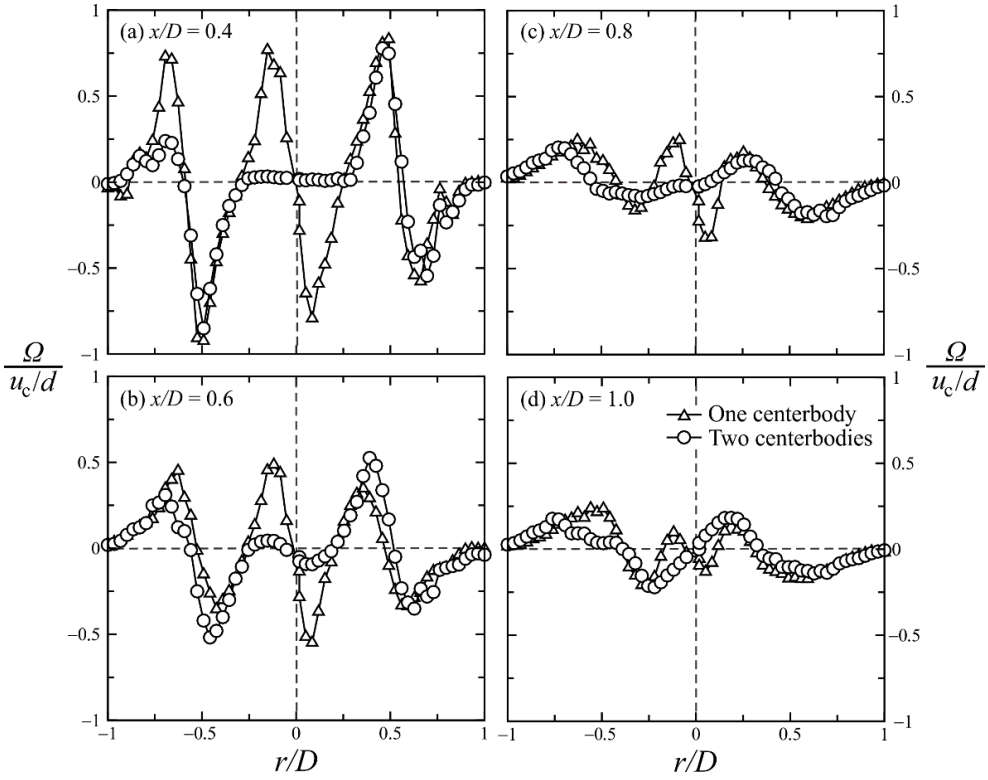

Figure 10. Radial distributions of time-averaged vorticity at x/D = (**a**) 0.4, (**b**) 0.6, (**c**) 0.8, and (**d**) 1.0. Re_c = 280, Re_a = 480, and S = 0.432.

Figure 11a,b present the normalized Lagrangian integral time scales of the axial $(\tau_{L,u}u_c/D)$ and radial $(\tau_{L,v}u_c/D)$ fluctuation velocities on the x-axis, respectively. In Figure 11a, the values of $(\tau_{L,u}u_c/D)$ in the one-centerbody case exhibit higher than those in the two-centerbodies case. Similar to what occurs in the x-axis of Figure 11a, the values of $(\tau_{L,v}u_c/D)$ observed in the one-centerbody case are smaller than those in the two-centerbodies case. In addition, the values of $\tau_{L,v}u_c/D$ in the two-centerbodies case present larger magnitudes compared to those in the one-centerbody case. The values of $(\tau_{L,u}u_c/D)$ and $(\tau_{L,v}u_c/D)$ of the two-centerbodies case exhibit large values because the vortex stretching influence on the x-axis is created by velocity gradients [34]. Because no reverse flow occurs downstream of the RZ as CD1 and CD2 are installed, the velocity gradients on the x-axis exhibit low values. Low velocity gradients cause small vortex sketching; therefore, low turbulent intensities are induced along the central line (in Figure 7c,d).

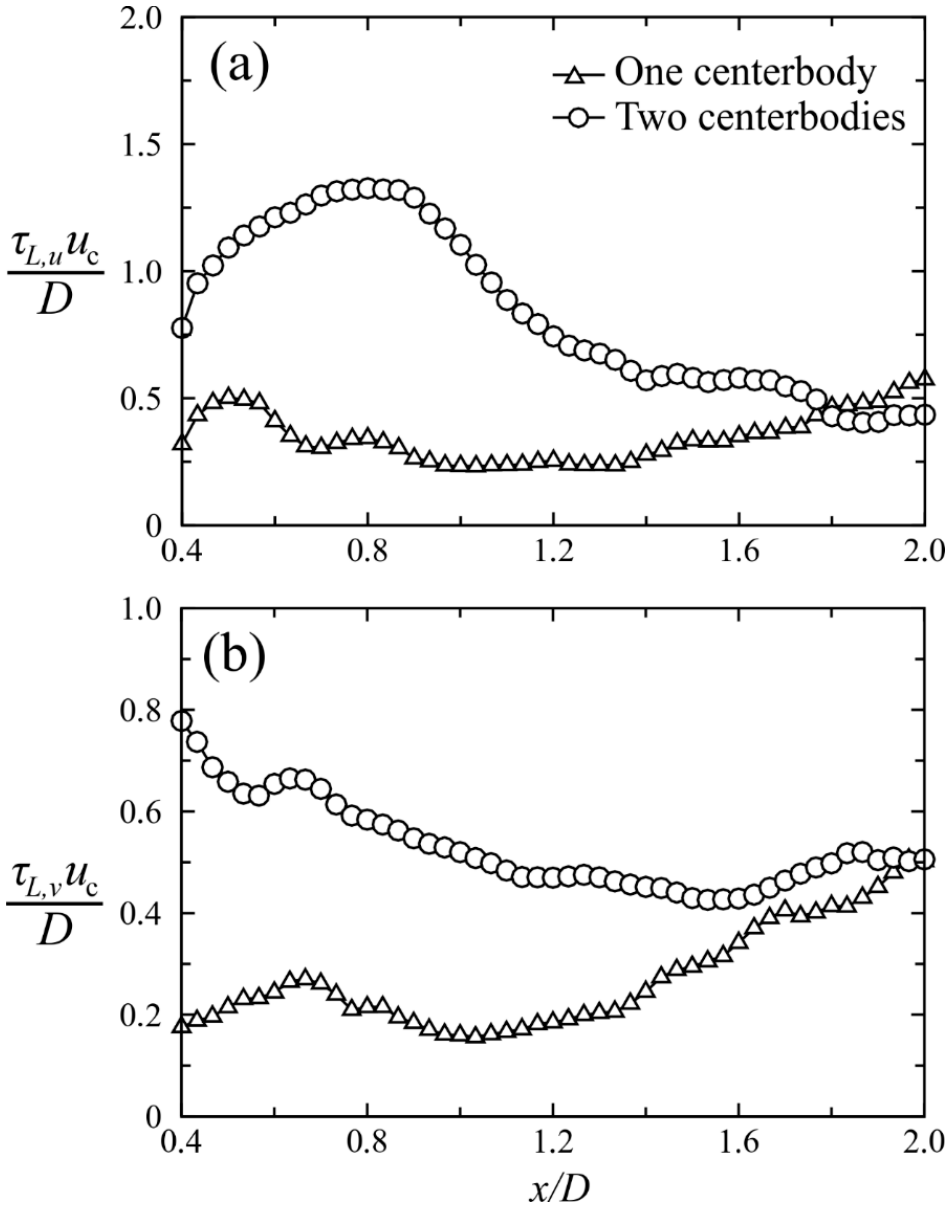

Figure 11. Normalized Lagrangian integral time scales of turbulence eddies along centerline. (**a**) Axial component, (**b**) radial component. Re_c = 280, Re_a = 480, and S = 0.432.

To transfer time-dependent measurement results to a spatial domain, the turbulent eddies' macro length scales in turbulent flow are estimated by applying Taylor's frozen flow field hypothesis to the Lagrangian integral time scales [34]. Taylor's hypothesis assumes that the time derivatives of flow properties can be obtained approximately from $\partial/\partial t = \overline{u}_i(\partial/\partial x_i)$, where t denotes time, x_i is the coordinate in the i direction, and $\overline{u}_i$ is the time-averaged local velocity component in the i direction. This relationship allows one to estimate spatial properties using temporal properties under the assumption that the turbulent eddies advected by the mean flow are sufficiently rapid that they do not have time to affect the properties substantially during the time they pass the point of observation. In this study, we assume that the local convective velocity is equal to the local time-averaged velocity. The axial and radial Lagrangian integral length scales are estimated by multiplying the Lagrangian integral time scales in Figure 11a,b by the local time-averaged velocities in Figure 7a,b, respectively. The normalized Lagrangian integral length scales of axial $(l_{L,u}/D)$ and radial $(l_{L,v}/D)$ turbulence eddies on the x-axis are presented in Figure 12a,b respectively. In the case of one centerbody, $(l_{L,u}/D)$ shown in

Figure 12a exhibits large values at $x/D < 0.8$ as a result of a great vortex stretching applied on the flow in the x-axis. In contrast, when CD2 is installed, as shown in Figure 12a, the values of $(l_{L,u}/D)$ exhibited in the case of one centerbody are relatively lower than those in the case of two centerbodies within the region $0.8 < x/D < 1.5$. In Figure 12b, $(l_{L,v}/D)$ on the x-axis of the two-centerbodies case presents smaller values than those in the one-centerbody case within $x/D < 2.0$. In general, the low values of $(l_{L,v}/D)$ exhibited in the wake are induced by small axial vortex stretching along the central axis [34].

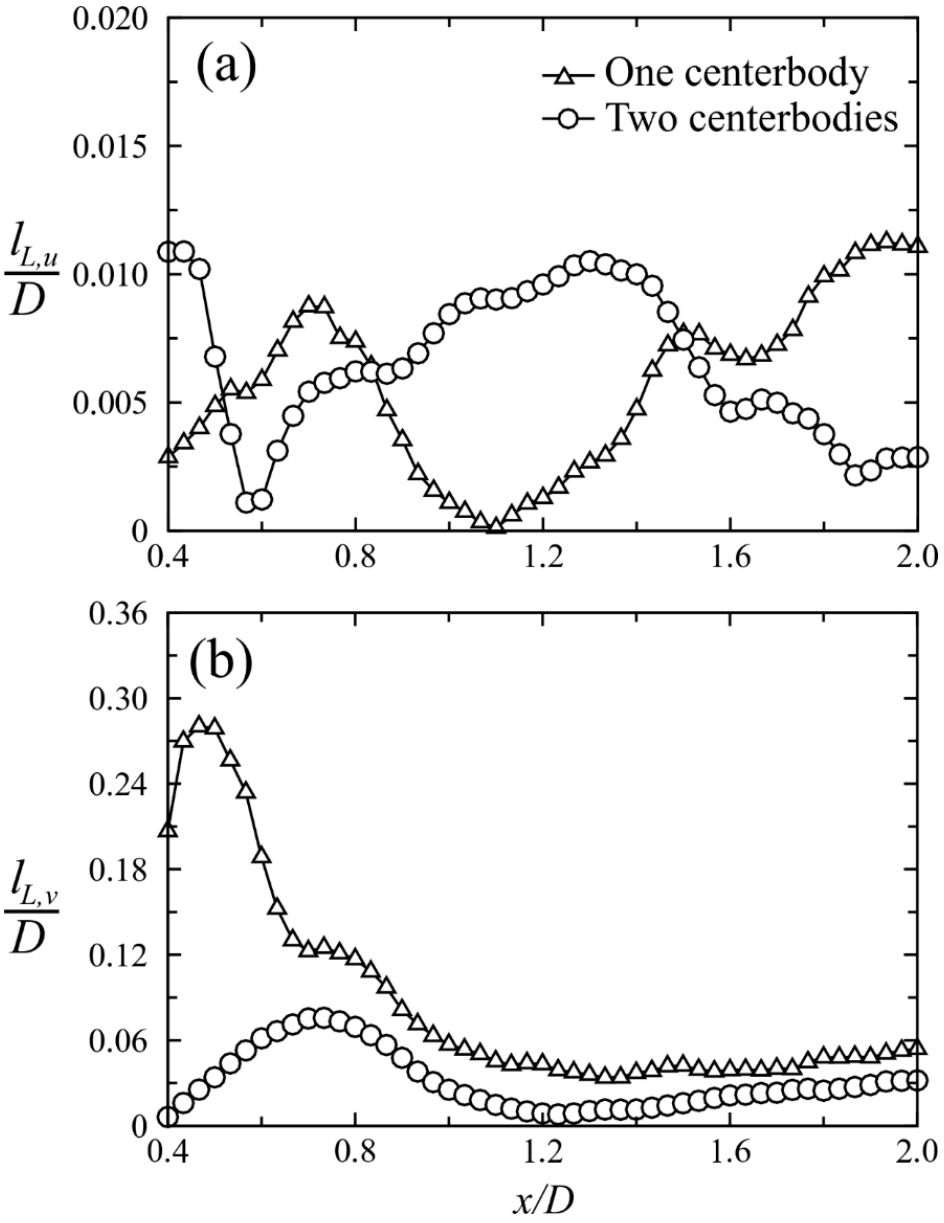

Figure 12. Normalized Lagrangian integral time length scales of turbulence eddies along centerline. (**a**) Axial component, (**b**) radial component. $Re_c = 280$, $Re_a = 480$, and $S = 0.432$.

4. Conclusions

The velocity characteristics of a swirling jet modulated by two centerbodies were studied experimentally. In this study, the flow patterns and velocity characteristics of swirling jets in the high turbulent swirling condition were presented for the range of annular jet Reynolds number $260 < Re_a < 700$ and swirl number $0.234 < S < 0.483$. The following conclusions were made from the study's findings and discussion.

- The turbulent forward-flow wake was found in the downstream wake in the case of using both CD1 and CD2. The forward flow existed immediately in the wake of the two centerbodies as varying the Rec and Rea.
- When CD1 was installed, there was no stagnation point or reversed-flow zone found along the x-axis of the jets. This was because a large momentum of the central jet fluids traveled quickly downstream after issuing from the central hole on CD1. A large RZ was induced as the annular jet passed CD1. Two stagnation points were found downstream of CD1 to associate two counter-rotating vortice pairs. A part of the central jet interacted with the annular swirling jet while most of those were going through the RZ. Using CD1 and CD2 to modify the wake of jets, the RZ was a combination of three pairs of counter-rotating vortices, i.e., two pairs were encapsulated between CD1 and CD2, while one pair was located downstream of CD2.
- Along the central jet axis, the strong swirling jet-like flow occurred downstream of the jets' wake, resulting in larger values of fluctuation intensities in the case of one centerbody compared to those in the case of two centerbodies. However, outside of the central jet column, the large values of radial fluctuation intensity in the case of two centerbodies occurred in longer and wider regions than those in the case of one centerbody.
- Although the turbulent forward-flow wake was formed in the case of using two centerbodies, the axial momentum of the central jet fluids transferred to the radial momentum due to the appearance of CD2. Hence, the radial fluctuation intensities were greater than those in the axial direction. This promotes a better mixing performance of the swirling double-concentric jets when two centerbodies are applied.

In future study, an analytical procedure with a numerical solution may be applied to investigate flow instability on the shear-layer vortices of swirling double-concentric jets as the central jet fluids pass through CD2, suggested by Shreen El-Sapa and co-workers [35–38], especially for flow at high central jet Reynolds numbers. This could help us to deeply understand the mixing characteristics of combined swirling jets' flow and large bluff bodies.

Author Contributions: Conceptualization, M.D.L.; methodology, M.D.L. and S.R.J.; software, M.D.L. and S.R.J.; validation, M.D.L. and S.R.J.; formal analysis, M.D.L.; investigation, M.D.L.; resources, M.D.L.; data curation, M.D.L. and S.R.J.; writing—original draft preparation, M.D.L.; writing—review and editing, M.D.L., D.N.D. and T.P.Q.N.; visualization, M.D.L. and S.R.J.; supervision, M.D.L.; project administration, M.D.L., D.N.D. and T.P.Q.N.; funding acquisition, M.D.L. and T.P.Q.N. All authors have read and agreed to the published version of the manuscript.

Funding: This research was partially funded by the Ministry of Education and Training, grant number B2020-DNA-01.

Institutional Review Board Statement: Not applicable.

Informed Consent Statement: Not applicable.

Data Availability Statement: Not applicable.

Acknowledgments: Special thanks go to Rong Fung Huang and Ching Min Hsu for their insightful comments and experimental procedure supports in the Thermal Science and Fluid Mechanics Laboratory, NTUST, Taiwan.

Conflicts of Interest: The authors declare no conflict of interest. The funders had no role in the design of the study; in the collection, analyses, or interpretation of data; in the writing of the manuscript; or in the decision to publish the results.

Nomenclature

A_a	area at exit of swirling jet (= $\pi(D_o^2 - D^2)/4$), 550 mm^2
A_c	area at exit of central jet (= $\pi d^2/4$), 19.6 mm^2
B	blockage ratio at exit of annular swirling jet (= D^2/D_o^2), 0.563
CD1	upstream centerbody
CD2	downstream centerbody
D	diameter of CD1, 30 mm
d	diameter of central jet at exit, 5 mm
D_c	diameter of CD2, 14 mm
D_h	hydraulic diameter of annular swirling jet at exit (= D_o–D), 10 mm
D_m	mean diameter for calculating swirl numbers (= $(D + D_o)/2$), 35 mm
D_o	outer diameter of annular swirling jet at exit, 40 mm
H	distance from CD1 to CD2, 10 mm
Re_a	Reynolds number of annular flow (= $u_a D_h/\nu$)
Re_c	Reynolds number of central jet (= $u_c d/\nu$)
r	radial coordinate
S	swirl number of annular jet
u	instantaneous axial velocity component
$\overline{u}$	time-averaged axial velocity
u'	root-mean-square of axial velocity fluctuations
u_a	mean axial velocity of annular swirling jet at exit (= Q_a/A_a)
u_c	mean axial velocity of central jet at exit (= Q_c/A_c)
v	instantaneous radial velocity component
$\overline{v}$	time-averaged radial velocity
v'	root-mean-square of radial velocity fluctuations
w	azimuthal velocity component
x	axial coordinate, originated from center of CD1
ν	kinematic viscosity of air, m^2/s

References

1. Caetano, N.R.; da Silva, L.F.F. A comparative experimental study of turbulent non premixed flames stabilized by a bluff-body burner. *Exp. Therm. Fluid Sci.* **2015**, *63*, 20–33. [CrossRef]
2. Huang, R.F.; Lin, C. Velocity fields of nonpremixed bluff-body stabilized flames. *J. Energy Resour. Technol.* **2000**, *122*, 88–93. [CrossRef]
3. Tang, H.; Yang, D.; Zhang, T.; Zhu, M. Characteristics of flame modes for a conical bluff body burner with a central fuel jet. *J. Eng. Gas Turbine Power* **2013**, *135*, 091507. [CrossRef]
4. Warda, H.; Kassab, S.; Elshorbagy, K.; Elsaadawy, E. An experimental investigation of the near-field region of free turbulent round central and annular jets. *Flow Meas. Instrum.* **1999**, *10*, 1–14. [CrossRef]
5. Chigier, N.A.; Bee'r, J.M. The flow region near the nozzle in double concentric jets. *J. Fluids Eng.* **1964**, *86*, 797–804. [CrossRef]
6. Luo, R.; Zhang, Y.; Li, N.; Zhou, Q.; Sun, P. Experimental study on flow and combustion characteristic of a novel swirling burner based on dual register structure for pulverized coal combustion. *Exp. Therm. Fluid Sci.* **2014**, *54*, 136–150. [CrossRef]
7. Patil, S.; Sahu, S. Air swirl effect on spray characteristics and droplet dispersion in a twin-jet crossflow airblast injector. *Phys. Fluids* **2021**, *33*, 073314. [CrossRef]
8. Rukes, L.; Sieber, M.; Paschereit, C.O.; Oberleithner, K. Effect of initial vortex core size on the coherent structures in the swirling jet near field. *Exp. Fluid* **2015**, *56*, 197. [CrossRef]
9. Saiki, Y.; Suzuki, Y.; Kasagi, N. Active control of swirling coaxial jet mixing with manipulation of large-scale vortical structures. *Flow Turbul. Combust.* **2011**, *86*, 399–418. [CrossRef]
10. Gupta, A.K.; Lilley, D.G.; Syred, N. *Swirl Flows*; Abacus Press: Tunbridge Wells, UK, 1984; 488p.
11. Leibovich, S. The structure of vortex breakdown. *Annu. Rev. Fluid Mech.* **1978**, *10*, 221–246. [CrossRef]
12. Markovich, D.M.; Dulin, V.M.; Abdurakipov, S.S.; Kozinkin, L.A.; Tokarev, M.P.; Hanjalić, K. Helical modes in low- and high-swirl jets measured by tomographic PIV. *J. Turbul.* **2016**, *17*, 678–698. [CrossRef]
13. Huang, R.F.; Lin, C.L. Flow characteristics and shear-layer vortex shedding of double concentric jets. *AIAA J.* **1997**, *35*, 887–892. [CrossRef]
14. Huang, R.F.; Tsai, F.C. Observations of swirling flows behind circular disks. *AIAA J.* **2001**, *39*, 1106–1112. [CrossRef]
15. Huang, R.F.; Tsai, F.C. Flow and mixing characteristics of swirling wakes in blockage-effect regime. *J. Wind Eng. Ind. Aerodyn.* **2004**, *92*, 199–214. [CrossRef]

16. Gupta, S.; Hemchandra, S.; Shimura, M.; Shanbhogue, S.; Ghoniem, A. Impact of a centrebody on the unsteady flow dynamics of a swirl nozzle: Intermittency of PVC oscillations. In Proceedings of the Turbomachinery Technical Conference and Exposition (ASME Turbo Expo 2021), Virtual Conference, 7–11 June 2021.
17. Huang, R.F.; Tsai, F.C. Flow field characteristics of swirling double concentric jets. *Exp. Therm. Fluid Sci.* **2001**, *25*, 151–161. [CrossRef]
18. Vanierschot, M.; Percin, M.; Van Oudheusden, B. Double helix vortex breakdown in a turbulent swirling annular jet flow. *Phys. Rev. Fluids* **2018**, *3*, 034703. [CrossRef]
19. Mansouri, Z.; Boushaki, T. Experimental and numerical investigation of turbulent isothermal and reacting flows in a non-premixed swirl burner. *Int. J. Heat Fluid Flow* **2018**, *72*, 200–213. [CrossRef]
20. Tong, Y.; Liu, X.; Wang, Z.; Richter, M.; Klingmann, J. Experiment and numerical study on bluff-body and swirl stabilized diffusion flames. *Fuel* **2018**, *217*, 352–364. [CrossRef]
21. Cozzi, F.; Sharma, R.; Solero, G. Analysis of coherent structures in the near-field region of an isothermal free swirling jet after vortex breakdown. *Exp. Therm. Fluid Sci.* **2019**, *109*, 109860. [CrossRef]
22. Sheen, H.; Chen, W.; Jeng, S. Recirculation zones of unconfined and confined annular swirling jets. *AIAA J.* **1996**, *34*, 572–579. [CrossRef]
23. Huang, R.F.; Yen, S. Axisymmetric swirling vortical wakes modulated by a control disk. *AIAA J.* **2003**, *41*, 888–896. [CrossRef]
24. Huang, R.F.; Duc, L.M.; Hsu, C.M. Effects of swirling strength on flow characteristics of swirling double-concentric jets with a dual-disk flow controller. *Exp. Therm. Fluid Sci.* **2015**, *68*, 612–624. [CrossRef]
25. Huang, R.F.; Duc, L.M.; Hsu, C.M. Flow and mixing characteristics of swirling double-concentric jets influenced by a control disc at low central jet Reynolds numbers. *Int. J. Heat Fluid Flow* **2017**, *62*, 233–246. [CrossRef]
26. Duc, L.M.; Huang, R.F.; Hsu, C.M. Swirling dual-disk double-concentric jets at low annulus Reynolds numbers. *Eur. J. Mech. B Fluids* **2017**, *61*, 33–45. [CrossRef]
27. Mei, R. Velocity fidelity of flow tracer particles. *Exp. Fluids* **1996**, *22*, 1–13. [CrossRef]
28. Zdravkovich, M. *Flow around Circular Cylinders*; Oxford University Press: Oxford, UK, 1997.
29. Filippa, L.; Freire, L.; Trento, A.; Álvarez, A.M.; Gallo, M.; Vinzón, S. Laboratory evaluation of two LISST-25X using river sediments. *Sediment Geol.* **2011**, *238*, 268–276. [CrossRef]
30. Boillot, A.; Prasad, A. Optimization procedure for pulse separation in cross-correlation PIV. *Exp. Fluids* **1996**, *21*, 87–93. [CrossRef]
31. Westerweel, J. Fundamentals of digital particle image velocimetry. *Meas. Sci. Technol.* **1997**, *8*, 1379. [CrossRef]
32. Steele, W.; Taylor, R.; Burrell, R.; Coleman, H. Use of previous experience to estimate precision uncertainty of small sample experiments. *AIAA J.* **1993**, *31*, 1891–1896. [CrossRef]
33. Luff, J.; Drouillard, T.; Rompage, A.; Linne, M.; Hertzberg, J. Experimental uncertainties associated with particle image velocimetry (PIV) based vorticity algorithms. *Exp. Fluids* **1999**, *26*, 36–54. [CrossRef]
34. Tennekes, H.; Lumley, J.L. *A First Course in Turbulence*; MIT Press: Cambridge, MA, USA, 1972.
35. El-Sapa, S. Interaction between a non-concentric rigid sphere immersed in a micropolar fluid and a spherical envelope with slip regime. *J. Mol. Liq.* **2022**, *351*, 118611. [CrossRef]
36. El-Sapa, S.; Faltas, M.S. Mobilities of two spherical particles immersed in a magneto-micropolar fluid. *Phys. Fluids* **2022**, *34*, 013104. [CrossRef]
37. Sherief, H.H.; Faltas, M.S.; El-Sapa, S. Axisymmetric creeping motion caused by a spherical particle in a micropolar fluid within a nonconcentric spherical cavity. *Eur. J. Mech. B Fluids* **2019**, *77*, 211–220. [CrossRef]
38. Sherief, H.H.; Faltas, M.S.; El-Sapa, S. Force on a spherical particle oscillating in a viscous fluid perpendicular to an impermeable planar wall. *J. Braz. Soc. Mech. Sci. Eng.* **2019**, *41*, 244. [CrossRef]